ARTICLES

Fe/Co Alloys for the Catalytic Chemical Vapor Deposition Synthesis of Single- and Double-Walled Carbon Nanotubes (CNTs). 1. The CNT−Fe/Co−MgO System

**Pierre Coquay,[†] Alain Peigney,[‡] Eddy De Grave,[†] Emmanuel Flahaut,[‡]
Robert E. Vandenberghe,[†] and Christophe Laurent*,[‡]**

*NUMAT, Department of Subatomic and Radiation Physics, University of Ghent, Proeftuinstraat 86, B-9000
Gent, Belgium, and CIRIMAT UMR CNRS-UPS-INP 5085, Centre Interuniversitaire de Recherche et
d'Ingénierie des Matériaux, Université Paul-Sabatier, 31062 Toulouse Cedex 9, France*

$Mg_{0.90}Fe_xCo_yO$ ($x + y = 0.1$) solid solutions were synthesized by the ureic combustion route. Upon reduction at 1000 °C in H_2−CH_4 of these powders, Fe/Co alloy nanoparticles are formed, which are involved in the formation of carbon nanotubes, which are mostly single and double walled, with an average diameter close to 2.5 nm. Characterizations of the materials are performed using ^{57}Fe Mössbauer spectroscopy and electron microscopy, and a well-established macroscopic method, based on specific-surface-area measurements, was applied to quantify the carbon quality and the nanotubes quantity. A detailed investigation of the Fe/Co alloys' formation and composition is reported. An increasing fraction of Co^{2+} ions hinders the dissolution of iron in the MgO lattice and favors the formation of $MgFe_2O_4$-like particles in the oxide powders. Upon reduction, these particles form α-Fe/Co particles with a size and composition (close to $Fe_{0.50}Co_{0.50}$) adequate for the increased production of carbon nanotubes. However, larger particles are also produced resulting in the formation of undesirable carbon species. The highest CNT quantity and carbon quality are eventually obtained upon reduction of the iron-free $Mg_{0.90}Co_{0.10}O$ solid solution, in the absence of clusters of metal ions in the starting material.

Introduction

Catalytic chemical vapor deposition (CCVD) methods are widely used for the synthesis of carbon nanotubes (CNTs) since they have a great potential for low-cost, large-scale production and furthermore offer the possibility to form the CNTs either inside a host material or very locally on patterned substrates. These methods, basically similar to those used for several decades for the synthesis of filamentous carbon, involve the catalytic decomposition of a carbonaceous gas (hydrocarbon or carbon monoxide) on transition-metal nanometric particles. Although several mechanisms do exist, CNTs with only one or two walls (SWNTs and DWNTs, respectively) are mainly produced by catalyst particles below ca. 3 nm in diameter.[1−4] Iron and cobalt have both found to be effective for the production of SWNTs and DWNTs, but several authors[5−8] have reported that Fe/Co alloys, sometimes referred to as bimetallic catalysts, are even more effective. The alloy formation or composition was not studied precisely, but the $Fe_{0.50}Co_{0.50}$ composition was nevertheless sometimes singled out as a particularly interesting one.[5,6,8] By contrast, the Fe/Co alloys involved in the formation of multiwalled CNTs (MWNTs).[9−16]

were often studied in greater detail, notably by Mössbauer spectroscopy[11−15] and X-ray photoelectron microscopy.[16] However, the size of these Fe/Co particles is much higher, in the range 20−40 nm, and the formation mechanisms of the MWNTs are different from those of the SWNTs and DWNTs. It was reported[11,12] that the most efficient alloy, in terms of stability toward oxidation and carburization reactions, has a composition close to $Fe_{0.50}Co_{0.50}$ and that avoiding the formation of Fe_3C was indeed beneficial for the formation of MWNTs. The latter point was also reported in the case of SWNTs and DWNTs.[4,7,17]

The present authors have proposed an original CCVD method[18] where pristine metal nanoparticles are formed in situ at a temperature high enough for them to catalyze the decomposition of CH_4 and the subsequent formation of CNTs. In this method, an oxide starting material is reduced in H_2−CH_4 atmosphere to produce a CNT−metal−oxide nanocomposite powder. The use of MgO as the oxide is advantageous since a simple soaking in HCl allows separation of the CNTs without damaging them.[2] The formation of the suitable metal nanoparticles is notably governed by the dispersion state of the corresponding ions in the starting oxide. In the case of (Mg, Fe)O,[19−21] Fe^{3+} ions well-dispersed in the octahedral (Oh) sites of MgO tend to form Fe^{2+} ions whose reduction rate to metallic iron is very low while clusters of Fe^{3+} ions and $MgFe_2O_4$-like particles are directly reduced to metallic iron. Poorly dispersed Fe^{3+} clusters and large $MgFe_2O_4$-like particles are mostly involved in the formation of thick carbon nanofibers, the outer

* To whom correspondence should be addressed. Tel: +33 (0)5 61 55 61 22. Fax: +33 (0)5 61 55 61 63. E-mail: laurent@chimie.ups-tlse.fr.
† NUMAT, Department of Subatomic and Radiation Physics, University of Ghent.
‡ CIRIMAT UMR CNRS-UPS-INP 5085, Centre Interuniversitaire de Recherche et d'Ingénierie des Matériaux, Université Paul-Sabatier.

diameter of which is determined by the particle size. By contrast, well-dispersed Fe^{3+} clusters and small $MgFe_2O_4$-like particles lead to small catalytic particles (<5 nm), which tend to form SWNTS and DWNTs with an inner diameter close to 2 nm. In the case of (Mg, Co)O,[2,3,22] composite powders in which 90% of the CNTs are SWNTs and DWNTs are obtained provided the presence of Co_3O_4 in the starting material is avoided.

In this context, we have performed a detailed investigation of the Fe/Co alloys involved in the formation of SWNTs and DWNTs. Characterizations are performed using notably [57]Fe Mössbauer spectroscopy and electron microscopy as well as a macroscopical method based on specific-surface-area measurements. This work presents results for the CNT−Fe/Co−MgO system. It builds on several papers dealing with (Mg, Fe)O oxides,[23,24] Fe−MgO,[25] and Fe/Co/Ni−MgO[26] composite powders and CNT−Fe−MgO[21] and CNT−Co−MgO[2,3,22] composite powders. Results for the CNT−Fe/Co−MgAl₂O₄ system will be reported in a companion paper.[27]

Experimental Section

Oxide Synthesis. The appropriate amounts of metal nitrates (magnesium, iron, and cobalt) were mixed with the desired quantity of urea (NH_2−CO−NH_2) in order to produce 2 g of oxide solid solutions with the desired formula $Mg_{0.90}Fe_{0.10}O$, $Mg_{0.90}Fe_{0.05}Co_{0.05}O$, $Mg_{0.90}Fe_{0.0333}Co_{0.0667}O$, $Mg_{0.90}Fe_{0.02}Co_{0.08}O$, and $Mg_{0.90}Co_{0.10}O$. Following earlier works,[19,22,24] the urea quantity was fixed at three times the so-called stoichiometric ratio (four times for the cobalt-free sample, henceforward called Fe10, to which frequent reference is made in what follows). The reagents were mixed with 3.3 mL of water. The mixture had to be continuously stirred and slightly warmed to get a clear homogeneous solution. The Pyrex dish containing the clear homogeneous solution was placed in a furnace preheated at 600 °C. The solution immediately started to boil and dehydrate. Then the combustion process itself took place, as detailed elsewhere.[22,24] The combustion product formed a consistent homogeneous light brown "cake" occupying the dish volume. This product was slightly manually ground to produce a powder. For the sake of brevity, the oxide powders will be referred to in the following as Fe10, Fe5Co5, Fe3.33Co6.67, Fe2Co8 and Co10, respectively.

Synthesis of CNT−Fe−MgO Nanocomposite Powders. The CNT−Fe−MgO nanocomposite powders were obtained by selective reduction in a H_2−CH_4 atmosphere of the oxide powders prepared by combustion. Typically, 1 g of oxide powder was spread in an alumina vessel so that the powder bed did not exceed 5 mm in thickness. The reaction was carried out at atmospheric pressure in a fixed-bed flow reactor. The proportion of CH_4 was 18 mol %, giving rise to supersaturation in the H_2−CH_4 atmosphere at temperatures required for the formation of the CNTs (above 700 °C). The gas flow was fixed at 15 L/h, and the gas mixture was dried on P_2O_5. The thermal cycle was the following: heating rate of 5 °C/min up to 1000 °C, no dwell at 1000 °C, cooling rate of 5 °C/min to room temperature (RT). For the sake of brevity, the CNT−Fe/Co−MgO nanocomposite powders will be referred to in the following as Fe10R, Fe5Co5R, Fe3.33Co6.67R, Fe2Co8R, and Co10R, respectively, where "R" stands for "reduced".

Characterization. A method based on carbon element analysis and specific-surface-area measurements[18,28] was used in order to characterize the composite powders at a macroscopic scale and thus produce quantitative data which are most useful to compare the different specimens. Parts of the CNT−Fe/Co−MgO powders were oxidized in air in order to eliminate the

carbon as required for the study. The specific surface areas of the powders obtained after reduction (S_n) and of the oxidized specimens (S_o) were measured by the BET method using N_2 adsorption at liquid N_2 temperature in a Micromeritics FlowSorb II 2300 apparatus. This instrument gives a specific-surface-area value from one point (i.e., one adsorbate pressure) and requires calibration. The reproducibility of the results was determined to be in the ±3% range. $\Delta S = S_n − S_o$ represents the quantity of CNTs.[18,28] The oxidation process was limited to 5 min at 700 °C to avoid the sintering of the matrix grains and coalescence of the particles, which could give rise to undervalued S_o values and thus overvalued ΔS values. The carbon content in the powders obtained after reduction (C_n) was determined by flash combustion with an accuracy of ±2%. Carbon traces of the order of 0.3 wt % were also detected in the specimens oxidized at 700 °C (C_o). $\Delta S/\Delta C$ with $\Delta C = C_n − C_o$ is considered to represent the quality of the deposited carbon, a higher quality parameter principally corresponding to more carbon in tubular form and/or CNTs with fewer walls and/or less bundled CNTs.[18,28] X-ray diffraction (XRD) patterns were recorded with a Siemens D501 diffractometer using Cu Kα radiation and were computer-analyzed with the GUFI 5.0 program.[23] For lattice-parameter measurements, the powders were mixed with NaCl as internal standard and the calculations were performed with the *UnitCell* program.[29] The crystallite sizes were evaluated from the widths at half-maximum of the diffraction peaks using the well-known Scherrer's formula, with an accuracy of the order of 20%.

Mössbauer spectra (MS) were recorded with a [57]Co (Rh) source using conventional time-mode spectrometers with a constant-acceleration drives and triangular-reference signals. Accumulation of the data was performed in 1024 channels until a background of at least 10^6 counts per channel was reached. The spectrometers were calibrated by collecting at RT the MS of a standard α-Fe foil and the isomer-shift values quoted hereafter are with reference to this standard. The measured absorbers were prepared with the amount of powder corresponding to 10 mg of iron atoms per square centimeter. For all samples, Mössbauer measurements were performed at RT and at 80 K. The spectra were generally analyzed assuming symmetrical components with Lorentzian line shapes. Alternatively, Mössbauer patterns were fitted with model-independent hyperfine-field and/or quadrupole-splitting distributions with Lorentzian-shaped elemental components, where linear correlations between the isomer shift, δ, and the quadrupole shift, $2\epsilon_Q$, on one hand, and the hyperfine field, H_{hf}, on the other hand (correlation coefficients D_δ and D_ϵ, respectively) of a distributed sextet, and between the isomer shift and the quadrupole splitting, ΔE_Q (correlation coefficient D_δ), of a distributed doublet, can be imposed.[30] For the oxide Fe5Co5, MS were additionally collected at various temperatures between 14 K and RT to retrieve more specific information about the nature of the precursor oxides in general.

The CNT−Fe/Co−MgO nanocomposite powders were examined with a JEOL JSM 6400 scanning electron microscope (SEM) and with a JEOL JEM 2010 transmission electron microscope (TEM). The latter microscope allows high-resolution images to be obtained where the fringes corresponding to the walls of isolated CNTs are clearly resolved. Moreover, using a short image-capture time, many images are obtained at different places of a sample in a short time. It is then possible to get meaningful results on the distribution of the CNTs number of walls and diameters in a powder. At least 70 individual CNTs per sample were considered in these distributions.

TABLE 1: Macroscopical Parameters of the CNTs−Fe/Co−MgO Nanocomposite Powders[a]

composite powder	S_{ss} (m²/g)	S_n (m²/g)	S_o (m²/g)	C_n (wt %)	C_o (wt %)	ΔS (m²/g)	$\Delta S/\Delta C$ (m²/g)
Fe10R	6.6 ± 0.2	8.0 ± 0.2	5.7 ± 0.2	3.5 ± 0.1	0.1	2.3 ± 0.4	68 ± 15
Fe5Co5R	7.6 ± 0.2	12.6 ± 0.4	8.0 ± 0.2	2.6 ± 0.1	0.3	4.6 ± 0.6	201 ± 35
Fe3.33Co6.67R	11.7 ± 0.3	17.0 ± 0.5	10.2 ± 0.3	3.6 ± 0.1	0.3	6.8 ± 0.8	209 ± 34
Fe2Co8R	15.7 ± 0.5	25.0 ± 0.8	17.0 ± 0.5	4.7 ± 0.1	0.4	8.0 ± 1.3	184 ± 36
Co10R	30.0 ± 0.9	51.7 ± 1.6	32.7 ± 1.0	4.6 ± 0.1	0.4	19.0 ± 2.5	452 ± 78

[a] S_{ss}, specific surface area of the oxide precursor; S_n, specific surface area of the nanocomposite powder; S_o, specific surface area of the oxidized nanocomposite powder (5 min at 700 °C in air); C_n, carbon content in the nanocomposite powder; C_o, carbon content in the oxidized nanocomposite powder; $\Delta S = S_n - S_o$, CNTs quantity parameter; $\Delta S/\Delta C$: carbon quality parameter ($\Delta C = C_n - C_o$).
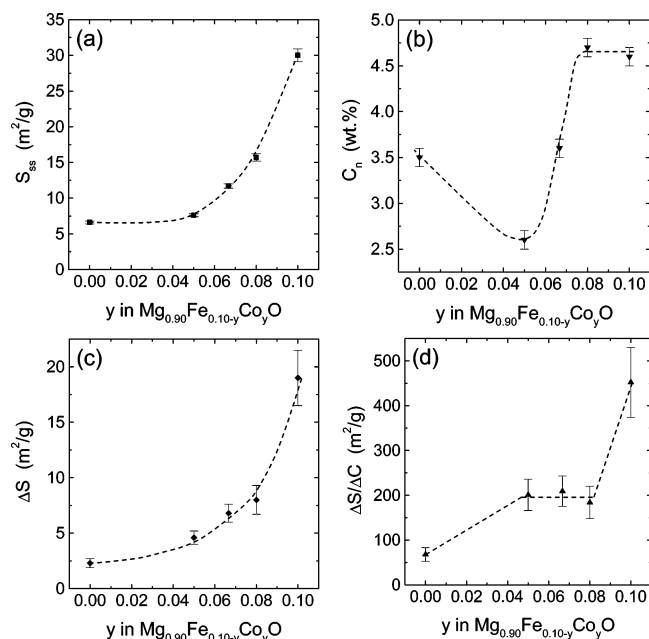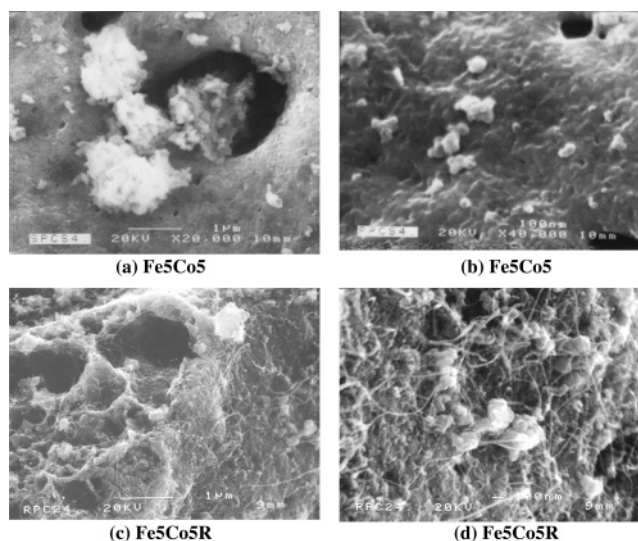

Figure 1. (a) Specific surface area S_{ss} of the oxide powders, (b) carbon content C_n, (c) CNT quantity parameter ΔS, and (d) carbon quality parameter $\Delta S/\Delta C$ of the CNTs−Fe/Co−MgO nanocomposite powders versus the cobalt proportion.

Figure 2. SEM images of Fe5Co5 (a, b) and Fe5Co5R (c, d).

Results

Carbon Content and Specific Surface Areas. The specific surface area S_{ss} of the oxide powders and the macroscopic parameters of the corresponding CNT−Fe/Co−MgO nanocomposite powders are shown in Figure 1 and Table 1. S_{ss} (Figure 1a) increases with the cobalt fraction in the oxide powder, with the steepest increase between Fe2Co8 and Co10. The carbon content C_n (Figure 1b) decreases from Fe10R to Fe5Co5R and then increases again to reach a plateau for Fe2Co8R and Co10R. The CNT-quantity parameter ΔS (Figure 1c) increases with the cobalt fraction, revealing a particularly large increase in the CNT quantity between Fe2Co8R and Co10R. $\Delta S/\Delta C$ (Figure 1d) increases from Fe10R to reach a plateau for Fe5Co5R, Fe3.33Co6.67R, and Fe2Co8R and then more than doubles for Co10R. Consequently, the higher carbon content in Fe10R as compared to Fe5Co5R probably results from the presence of more undesirable carbon species, as opposed to CNTs, in the former sample. It appears also that the increase of the carbon content from Fe5Co5R to Fe2Co8R is associated with a proportional increase in the quantities of CNTs and other undesirable carbon species, so that the carbon quality remains constant. Co10R presents by far the best results as far as both CNT quantity and carbon quality are concerned.

Electron Microscopy. SEM images of Fe5Co5 and of Fe5Co5R, which are typical of the samples containing iron and cobalt, are shown in Figure 2. Fe5Co5 (Figure 2a,b) consists of two types of grains. The first type consists of grains that have experienced a high degree of sintering. They form a foam that is more compact than the one observed for Fe10,[24] but with large open cavities. The second kind of grains, ranging in size from about 100 nm to several micrometers, are loose agglomerates of smaller crystallites and are dispersed on the surface of the foam. energy-dispersive X-ray analysis with a beam diameter of the order of 1 μm reveals similar proportions of iron and cobalt in both types of grains, the relative proportions of iron and cobalt being more or less equivalent, as aimed at for this particular composition. In Fe5Co5R (Figure 2c,d), the oxide matrix keeps a similar aspect as compared to the oxide before reduction, but carbon filaments, typical of CNT bundles, cover the surface of all grains.

Typical TEM images of the CNT−Fe/Co−MgO nanocomposite powders are presented in Figure 3. Figure 3a shows the presence of metal particles (dark spots) in Fe5Co5R, which, when examined at higher magnification (Figure 3b), are observed to be covered by graphene sheets that frequently exhibit deformations, possibly arising from aborted nucleation of CNTs. Figure 3c depicts a bundle of CNTs. In Figure 3d, a thin DWNT is leaving (or joining) a bundle. Some disordered carbon appears at the intersection. Figure 3e reveals a bent SWNT with a metal particle, about 4 nm in diameter, at its tip. Figure 3f presents a picture of a DWNT with a defect resulting in a bulge in the tube. Such CNTs were frequently observed in these samples. Figure 3g, referring to Fe3.33Co6.67R, shows a carbon nanocapsule without a metal particle inside, which is, however, very rare in these samples. Finally, in Figure 3h one notices the appearance of some thick carbon fibers partially filled with metal and similar to those observed for CNT−Fe−MgO powders.[21] However, they are much less abundant in the present cobalt-containing samples.

Figure 4 shows the particle-size, the number-of-walls, the SWNT-diameter, and the DWNT-inner-diameter distributions
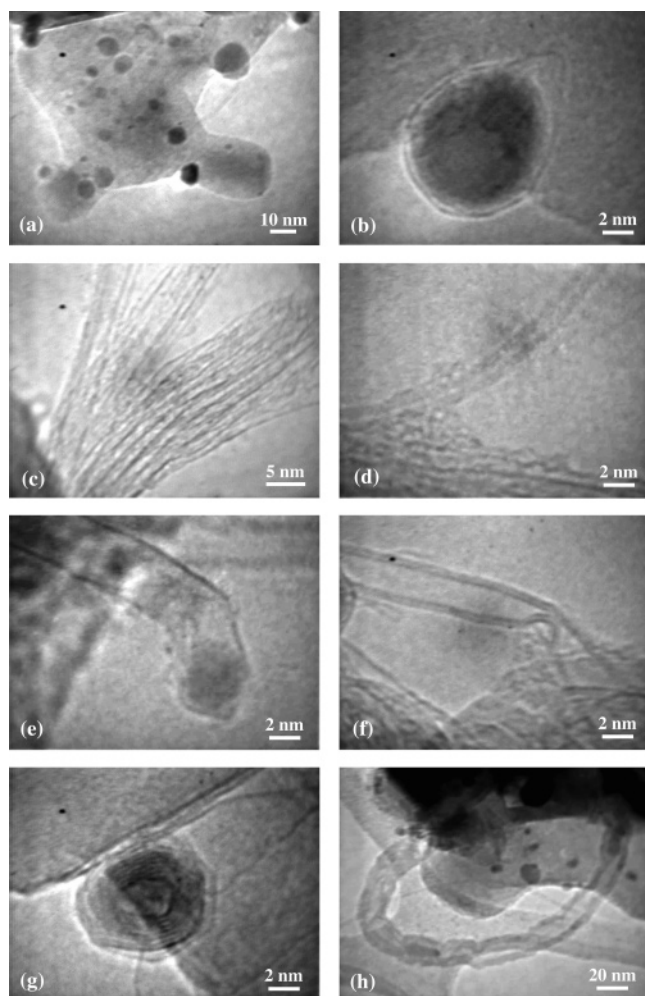
Figure 3. TEM images of Fe5Co5R (a, b, c, f, g) and Fe3.33Co6.67R (d, e, h).

in Fe5Co5R, a typical example of the CNT−Fe/Co−MgO nanocomposite powders. The particle-size distribution (Figure 4a) reveals that 90% of the particles are smaller than 10 nm and no particles with a diameter higher than 20 nm are observed. The average particle diameter is equal to 6.0 nm. It is to be noted that the proportion of small particles (<5 nm diameter) is probably underestimated due to the difficulty to detect them compared to larger particles. Moreover, most of the probed particles are not associated with CNTs. However, they can be considered representative of the general trend of the particle-size distribution in a particular sample. As reported elsewhere[21] the particle-size distribution in Fe10R is drastically broader with a maximum particle diameter of about 60 nm. The average Fe10R particle diameter (8.3 nm) is, however, similar to the presently obtained value for Fe5Co5R. For Co10R, the particle size distribution is narrower with a maximum particle diameter of about 10 nm, the average particle diameter being about 4 nm, as estimated from other works.[19,22]

More than 85% of the CNTs are SWNTs and DWNTs (Figure 4b). The width of the diameter distributions for the SWNTs (Figure 4c) is similar to that (1−5 nm) reported for SWNTs prepared by catalytic methods[1−3,6,31−36] and reflects a mechanism in which the diameter is established by the catalytic particle.[33,37] As observed for CNT−Fe−MgO[17,21] and CNT−Fe−Al$_2$O$_3$ specimens,[4,38] a higher proportion of the inner diameters is within the smallest diameter class for the DWNTs than for the SWNTs (parts c and d of Figure 4), resulting in a smaller average inner diameter for the DWNTs than for the SWNTs

(2.2 and 2.6 nm, respectively). This could reflect either the internal growth of the second wall, possibly by the yarmulke mechanism,[33] or a higher activity of the small catalytic particles for DWNT formation.

X-ray Diffraction. The XRD patterns of Fe5Co5, Fe3.33-Co6.67, Fe2Co8, Co10, and the corresponding nanocomposite powders are presented in Figure 5. The XRD spectra for Fe10 and Fe10R were reported earlier.[21,24] All patterns show the five peaks characteristic of MgO. From the positions of these peaks, the MgO-lattice parameters were calculated[29] (Table 2), and from their widths at half-maximum, the average crystallite sizes were estimated using the well-known Scherrer formula (Table 2). No Co$_3$O$_4$ was detected, and the main peak of MgFe$_2$O$_4$ is very weak for Fe5Co5, Fe3.33Co6.67, and Fe2Co8 (Figure 5a) but its appearance confirms the presence of MgFe$_2$O$_4$-like particles in these oxides. For Co10, however, no phase other than MgO is detected in the XRD analysis, indicating that the desired stoichiometry Mg$_{0.9}$Co$_{0.1}$O was probably established.[19,22] Mg$_{1-x}$Co$_x$O form ideal solid solutions which follow Vegard's law.[39] However, several authors[23,40−42] have shown that Mg$_{1-x}$Fe$_x$O solid−solution members instead exhibit a positive shift from the ideal linear correlation between a and x. Hence, it is difficult to quantitatively interpret the lattice parameters of MgO containing iron and cobalt ions in terms of substitution degree. For Fe10, the lattice parameter, according to Vegard's law, would correspond to only 5 atom % iron in solution in MgO,[24] while for Co10 the value is similar to the one reported[39] for a Mg$_{0.90}$Co$_{0.10}$O solid solution (0.4218 ± 0.0002 nm).

All the MgO-lattice parameters are higher in the CNT−Fe/Co−MgO nanocomposite powders than in the corresponding oxide precursors (Table 2), inferring that upon reduction a larger fraction of the iron and/or cobalt ions have entered the MgO lattice substituting for magnesium ions. The ionic radii of Fe^{2+} and Co^{2+} are indeed about 10% larger than the ionic radius of Mg^{2+}. It appears also that the MgO-lattice parameter of Co10R is close to that of Co10. These findings suggest that a high proportion of the Co^{2+} ions substituting in the precursor MgO structure have not been reduced to metallic cobalt and have remained embedded in the MgO lattice.

The average MgO-crystallite sizes are similar for oxide and nanocomposite powders. They are significantly larger for the powders containing iron than for Co10 and Co10R, which is in line with the results for the specific-surface areas S_{ss} (Figure 1a and Table 1). So far, the reason for the effect of Co substitution upon the size of the MgO grains has remained unclear.

Contrary to Fe10R,[21] neither α-Fe nor Fe$_3$C is detected in the XRD patterns of Fe5Co5R, Fe3.33Co6.67R, and Fe2Co8R (Figure 5b). Besides MgO, only α-Fe/Co is detected in these samples and, according to the intensity of the diffraction line near $2\theta = 45°$, its content increases with the cobalt fraction. In Co10R, only face-centered cubic (fcc) Co is detected. A weak peak characteristic of the distance between two graphene sheets in MWNTs and/or in graphite is observed except in Co10R. In the latter pattern, however, this peak could be masked by the intense signal at low angles coming from the powder support used during the measurement.

^{57}Fe Mössbauer Spectroscopy. *The Precursor Oxide Powders.* Typical MS for the Fe5Co5 oxide powder are reproduced in Figure 6. They were fitted similarly to those of Fe10[24] with a superposition of a (super)paramagnetic Fe^{2+} quadrupole-splitting distribution (QSD), a (super)paramagnetic Fe^{3+} QSD, and, below 200 K, in addition a magnetic hyperfine-field distribution (HFD) which closely resembles the "MgFe$_2$O$_4$-like"

CCVD Carbon Nanotubes in CNT−Fe/Co−MgO

*J. Phys. Chem. B, Vol. 109, No. 38, 2005* **17817**
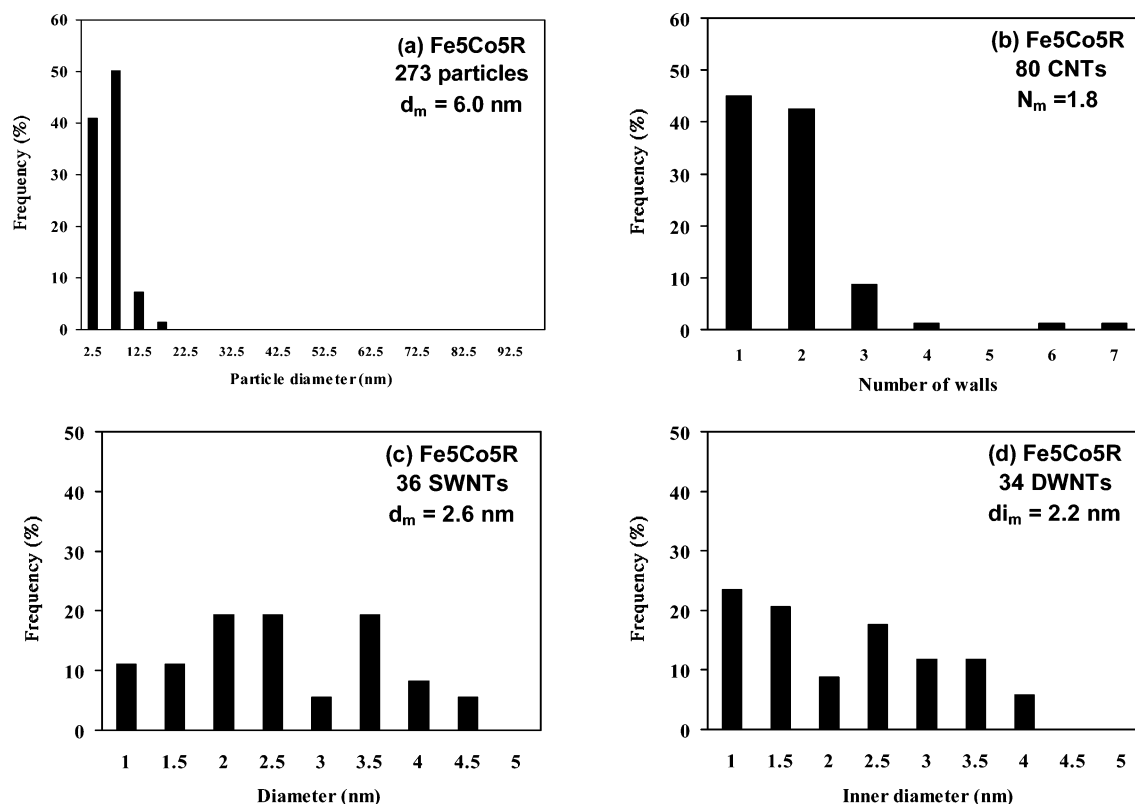
Figure 4. Particle size (a), number of walls (b), SWNT diameter (c), and DWNT inner diameter (d) distributions in Fe5Co5R, measured on TEM images (typically as those shown on Figure 3). Each class noted by a value x nm corresponds to particle sizes contained between $x - 2.5$ nm and $x + 2.5$ nm or to CNT (inner) diameters contained between $x - 0.25$ nm and $x + 0.25$ nm. For all distributions, the number of measurements and the average value are given (N_m, d_m, di_m).

distribution observed for the Fe10 oxide. The as such obtained Mössbauer parameters for different temperatures between 14 K and RT are listed in Table 3.

The Fe^{2+} QSD profile at low temperatures, $T \leq 250$ K, shows two clearly distinct maxima (Figure 6b,f), indicating the presence of two different sites for the ferrous species. For both sites the maximum-probability quadrupole splitting ΔE_Q is rather low for ferrous species. For the Fe^{2+} site with the largest, low-temperature splitting the value of ΔE_Q rapidly decreases with increasing temperature (see Table 3), whereas for the other Fe^{2+} site there is an initial increase up to ~75 K, followed by a gradual lowering at higher temperatures. As a result of the different temperature evolution of ΔE_Q the two ferrous components at room temperature (RT) can no longer be resolved. Again, this behavior is very similar to what is observed for the Fe^{2+} QSD component evaluated from the MS of the Fe10 precursor oxide in the preceding work of Coquay et al.,[17] where the two QSD maxima were attributed to isolated (lowest ΔE_Q at 14 K) and clustered Fe^{2+} ions in Oh sites of the MgO structure, respectively. That assignment was based on several earlier, independent reports[23,43−48] on $(Mg_{1−x}Fe_x)O$ solid solutions. The distinct temperature variations of the quadrupole splitting may then be attributed to different crystal fields acting at the respective sites.

The calculated Fe^{3+} QSD profile at RT displays three maxima (Table 3 and Figure 6k). It should be mentioned that an equally adequate fit was obtained with three discrete, independent, Lorentzian-shaped doublets (results labeled RTbis in Table 3) in addition to the ferrous QSD. The first maximum in the Fe^{3+} QSD profile (lowest maximum-probability ΔE_Q) could be attributed to ferric species in the Oh sites of MgO, or possibly in the Oh sites of a $MgFe_2O_4$ structure.[44,46,49] The second doublet component has a similar δ but a larger ΔE_Q and may arise from
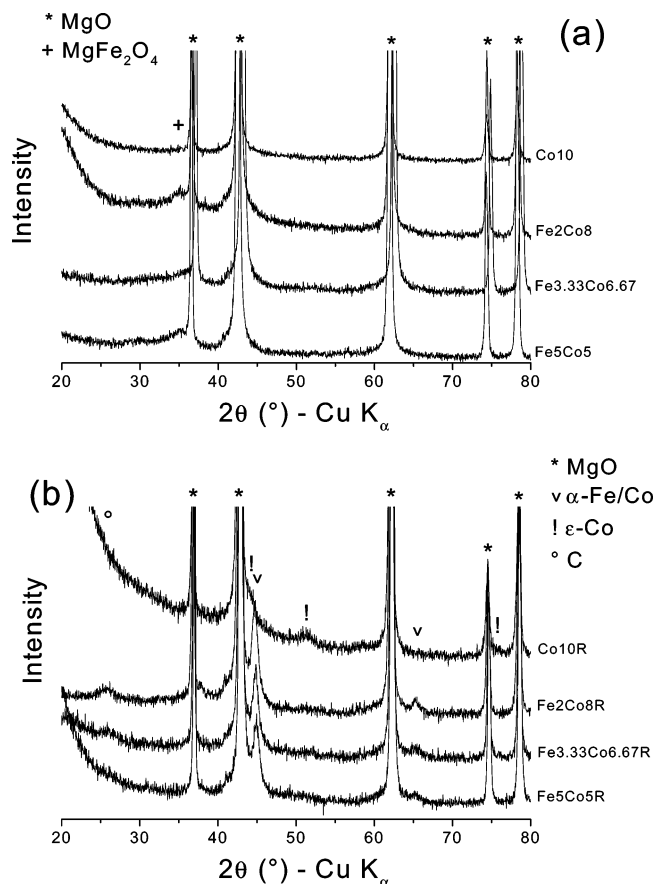
Figure 5. XRD patterns of Fe5Co5, Fe3.33Co6.67, Fe2Co8, Co10 (a) and of the corresponding nanocomposite powders (b).
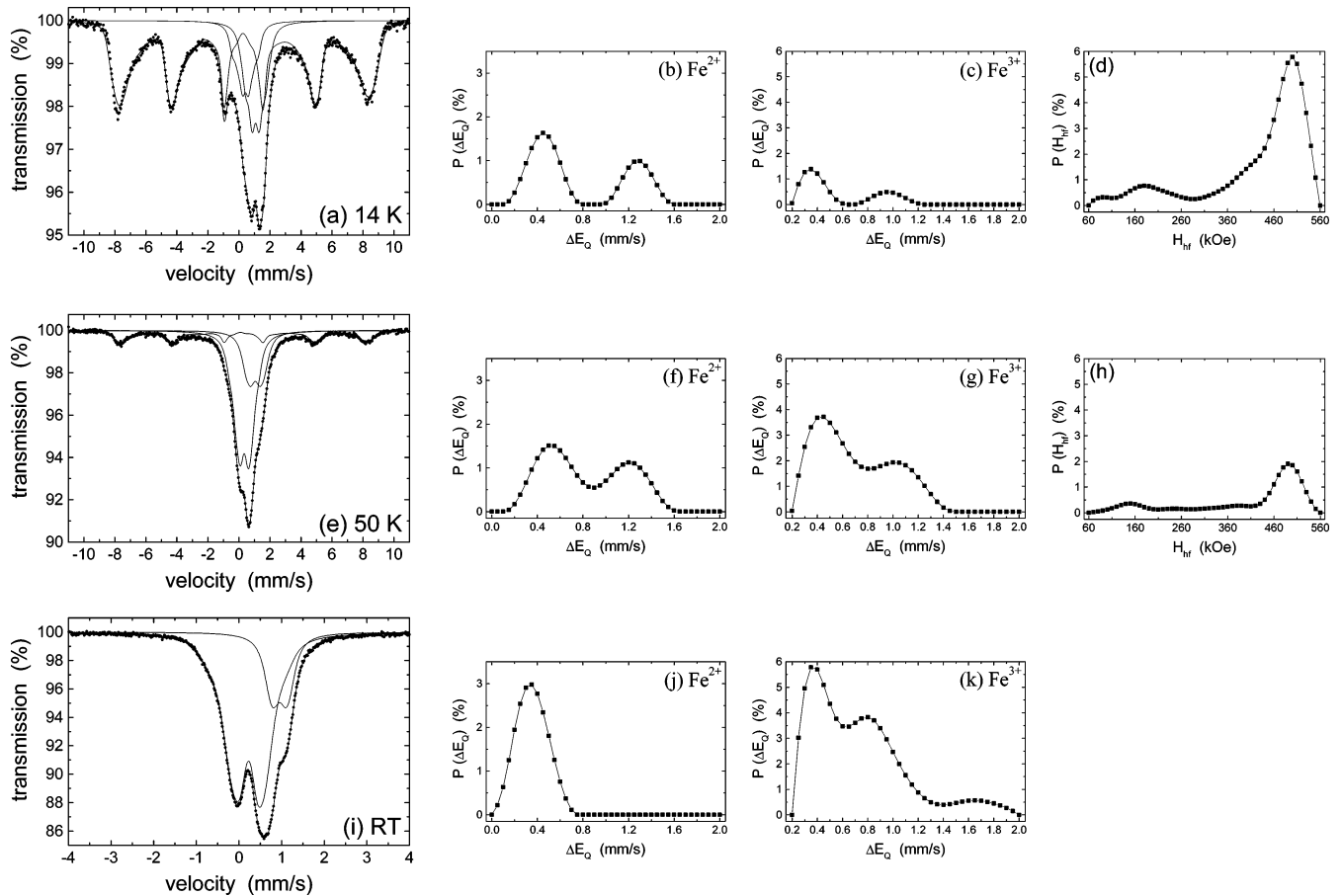
Figure 6. Mössbauer spectra of Fe5Co5 measured between 14 K and RT (a, e, i) and corresponding quadrupole-splitting distributions of the (super)paramagnetic Fe^{2+} phases (b, f, j), quadrupole-splitting distributions of the (super)paramagnetic Fe^{3+} phases (c, g, k), and hyperfine-field distributions of the magnetic $MgFe_2O_4$-like phase (d, h).

TABLE 2: MgO Lattice Parameter (*a*) and Average MgO Crystallite Size (Ø) of Fe10R, Fe5Co5R, Fe3.33Co6.67R, Fe2Co8R, Co10R, and of the Corresponding Oxide Precursors

composite powder	*a* (oxide) (nm)	*a* (composite) (nm)	Ø (oxide) (nm)	Ø (composite) (nm)
Fe10R	0.4221 ± 0.0004	0.4226 ± 0.0004	52.2 ± 10.4	58.3 ± 11.7
Fe5Co5R	0.4214 ± 0.0001	0.4221 ± 0.0002	69.6 ± 13.9	64.6 ± 12.9
Fe3.33Co6.67R	0.4215 ± 0.0001	0.4220 ± 0.0003	71.5 ± 14.3	71.8 ± 14.4
Fe2Co8R	0.4216 ± 0.0001	0.4219 ± 0.0002	61.2 ± 12.2	62.3 ± 12.5
Co10R	0.4216 ± 0.0001	0.4217 ± 0.0002	35.8 ± 7.2	31.6 ± 6.3

Oh Fe^{3+} ions forming clusters in the MgO structure. The shallow, third ferric component has an even larger ΔE_Q, but a smaller δ and could therefore be assigned to Fe^{3+} ions at interstitial tetrahedral (Td) sites in the MgO structure,[49] thus reflecting the presence of clusters, or to Fe^{3+} ions at tetrahedral sites in nanosized $MgFe_2O_4$-like particles.[46,49] This latter assignment would be consistent with the XRD patterns (Figure 5a), which indeed indicate the presence of a $MgFe_2O_4$-like phase in the involved Fe5Co5 oxide powder. Since the assignment of the distinct ferric components is not straightforward and hence may be questioned, the authors in the present contribution will henceforward refer to two octahedral Oh sites, Oh(I) and Oh(II), respectively, and one tetrahedral Td site for the Fe^{3+} cations, without being specific regarding the true nature of the Oh sites.

The third maximum in the Fe^{3+} QSD profiles (Td sites) is not present at temperatures $T \leq 150$ K (Figure 6c,g), the same temperatures at which a magnetic component appears in the MS. In contrast, the first and second maxima in the Fe^{3+} QSD profile remain present down to temperatures as low as 14 K (Figure 6c). However, their combined contribution (parameter *P* in Table 3) to the total spectrum below ~150 K gradually

decreases with decreasing temperature, in favor of the magnetic component. Consequently, the third maximum and part of the first and/or the second maximum therefore may be interpreted as being due to $MgFe_2O_4$ particles that behave superparamagnetically at relatively high temperatures.

The magnetic part of the MS was described as a hyperfine-field distribution in the range 60−560 kOe, with the line-area ratios of the elemental sextets always being fixed at 3:2:1 (Table 3 and Figure 6d,h). Adjustable, linear correlations between the isomer shift and hyperfine field and between the quadrupole shift and hyperfine field, with correlation coefficients D_δ and D_ϵ, respectively, allowed to account for the asymmetry, clearly observed at low temperatures, of the magnetic pattern. At intermediate temperatures, the magnetic component has become too weak to produce coherent D_δ and D_ϵ parameters, and no correlations were imposed. The average Mössbauer parameters corresponding to the maximum of the hyperfine-field distributions for the various temperatures (see Table 3) are in good agreement with those expected for $MgFe_2O_4$-like particles undergoing superparamagnetic relaxation.[50] It is to be noted that the extracted HFDs at low temperatures (Figure 6d,h) seem to contain a small contribution from a low-field component

TABLE 3: Mössbauer Parameters of Fe5Co5 Measured between 14 K and RT.

T (K)	(super)para Fe^{2+}				(super)para Fe^{3+}					magnetic $MgFe_2O_4$-like						
	δ	ΔE_Q[b]	Γ	P	δ	ΔE_Q[c]	D_δ	Γ	P	δ	H_{hf}[d]	$2\epsilon_Q$	D_δ	D_ϵ	Γ	P
		0.45			0.53	0.35										
14	1.18		0.49	19			0.0084	0.47	12	0.42	500	0.02	−0.0006	−0.0010	0.36	69
		1.30			0.52	0.95										
		0.49			0.46	0.45										
30	1.17		0.48	23			0.0438	0.52	29	0.41	497	0.01	−0.0005	−0.0007	0.30	48
		1.30			0.43	1.15										
		0.52			0.46	0.43										
50	1.16		0.64	24			0.0194	0.55	55	0.41	492	0.01	−0.0010	−0.0007	0.36	21
		1.20			0.44	1.00										
		0.59			0.48	0.42										
75	1.11		0.43	21			0.0333	0.47	66	0.42	486	−0.01	−0.0017	−0.0012	0.39	13
		1.15			0.46	0.95										
		0.43			0.49	0.39										
100	1.09		0.39	22			0.0440	0.48	70	0.41[e]	475	0.01[e]	0.0[e]	0.0[e]	0.25	8
		1.14			0.46	1.05										
					0.48	0.37										
		0.36														
150	1.09		0.35	20	0.47	1.00	0.0176	0.45	76	0.40[e]	461	0.01[e]	0.0[e]	0.0[e]	0.23	4
		0.95														
					0.46	1.60										
					0.42	0.35										
		0.23														
200	1.06		0.32	20	0.39	0.90	0.0483	0.47	80							
		0.62														
					0.37	1.45										
					0.35	0.35										
		0.16														
250	1.08		0.29	21	0.34	0.90	0.0124	0.48	79							
		0.70														
					0.32	1.55										
					0.34	0.37										
RT	1.06	0.34	0.34	22	0.33	0.80	0.0217	0.36	78							
					0.30	1.65										
					0.34	0.48		0.45	43							
RT bis[f]	1.07	0.34	0.38	22	0.31	0.90		0.47	31							
					0.27	1.72		0.36	4							

[a] para, paramagnetic; H_{hf}, maximum-probability hyperfine field (kOe); δ, (average) isomer shift (mm/s); ΔE_Q, maximum-probabilty quadrupole splittings (mm/s); $2\epsilon_Q$, (average) quadrupole shift (mm/s); Γ, Lorentzian line width (mm/s) of elemental doublet or sextet; P, proportion (%). D_δ and D_ϵ are the correlation coefficients between isomer shift and field and between quadrupole shift and field, respectively. [b] Quadrupole-splitting distribution from 0.00 to 2.00 mm/s. [c] Quadrupole-splitting distribution from 0.20 to 2.00 mm/s. [d] Hyperfine-field distribution from 60 to 560 kOe. [e] Fixed parameter. [f] Fit with three discrete, Lorentzian-shaped doublets.

(maximum at ∼125 kOe at 14 K), which could arise from magnetically ordered Fe^{2+} clusters in the MgO structure. However, an artifact from the fitting cannot be excluded.

To demonstrate the influence of the Fe/Co proportions, the MS of Fe10, Fe5Co5, Fe3.33Co6.67, and Fe2Co8 measured at RT are reproduced in Figure 7 and the corresponding Mössbauer parameters are listed in Table 4. A superposition of an Fe^{2+} quadrupole-splitting distribution and three discrete, independent Fe^{3+} quadrupole doublets yielded adequate fits. The assignment of these latter doublets, however, remains problematical.

The proportions of the different iron sites versus the cobalt fraction in the oxide powders are presented in Figure 8a. The proportion of substitutional Oh Fe^{2+} progressively decreases when iron is replaced by cobalt. This observation is in line with the well-known empirical law that Co^{2+} has a more distinct preference for 6-fold oxygen coordination than Fe^{2+} does. Hence, as more and more cobalt enters the play, proportionally less of the available iron as Fe^{2+} will substitute for Mg^{2+} in the MgO structure. Apparently, this lowering of the substitutional Oh Fe^{2+} fraction is accompanied by an increase of the proportion of Td Fe^{3+} species which are associated to $MgFe_2O_4$-like particles. This finding suggests that the presence of Co^{2+} cations triggers the formation of nanosized magnesium ferrite

phase. The combined fraction of the Oh ferric ions at first increases significantly but reverses its climb for Fe2Co8. This behavior is not well understood.

Dividing the iron proportions in Fe10, Fe5Co5, Fe3.33Co6.67, and Fe2Co8 (values from Table 4) by 1, 2, 3, and 5, respectively, allows comparison of the amounts of the different iron phases in oxide powders, as presented in Figure 8b. The amounts of Oh Fe^{2+} and Oh Fe^{3+} decrease with increasing cobalt fraction. However, the amount of Td Fe^{3+} lowers. It can thus again be suggested that the increase of the cobalt fraction in the oxide powders results in an increase of the amount or/and of the size of $MgFe_2O_4$-like particles, while the global amount of iron decreases.

The Composite Powders. Figure 9 shows the MS of Fe10R, Fe5Co5R, Fe3.33Co6.67R, and Fe2Co8R measured at RT. Four different phases are detected in all the involved CNT−Fe/Co−MgO nanocomposite powders. Their Mössbauer parameters at RT and at 80 K are given in Table 5 and Table 6, respectively.

The first phase, denoted *para Fe^{2+}* in Tables 5 and 6, refers to a nonmagnetic phase exhibiting a QSD (Figure 9d,g,j) similar to the one observed earlier for Fe10R (Figure 9b), where it was attributed to Fe^{2+} ions in the Oh sites of MgO. The fractional areas P of the Fe^{2+} QSDs are equal for the RT and 80 K spectra,
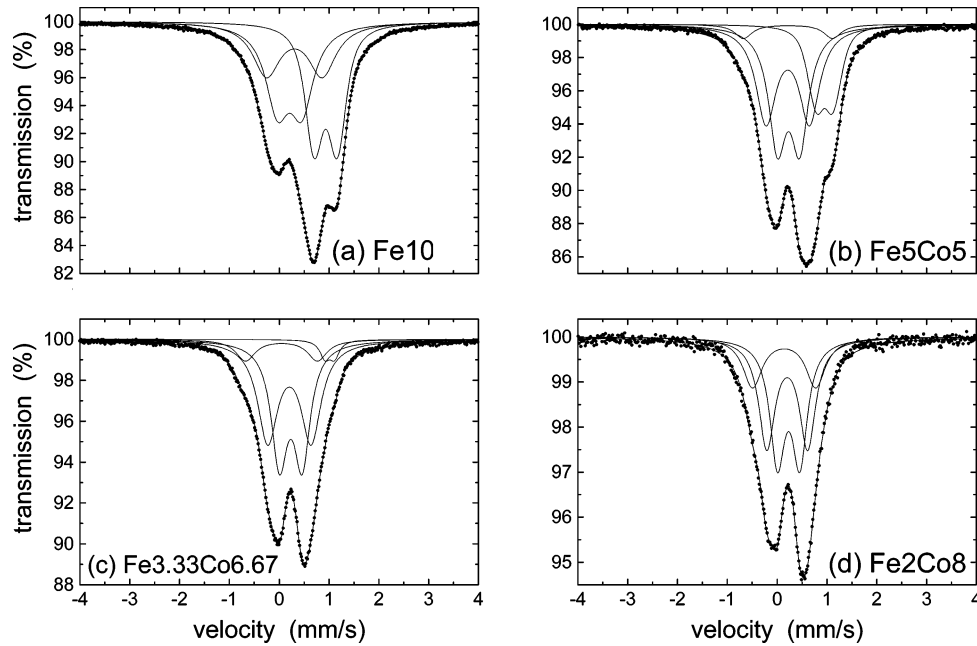
Figure 7. Mössbauer spectra of Fe10 (a), Fe5Co5 (b), Fe3.33Co6.67 (c), and Fe2Co8 (d) measured at RT. Three discrete, independent Lorentzian doublets, superimposed on an Fe^{2+} quadrupole-splitting distribution, were considered to characterize the Fe^{3+} phases.

TABLE 4: Mössbauer Parameters of Fe5Co5, Fe3.33Co6.67, and Fe2Co8 Measured at RT[a]

oxide powder	Oh Fe^{2+}				Oh Fe^{3+} [b]				Oh Fe^{3+} [c]				Td Fe^{3+}			
	δ	ΔE_Q	Γ	P	δ	ΔE_Q	Γ	P	δ	ΔE_Q	Γ	P	δ	ΔE_Q	Γ	P
Fe10	*1.04*	*0.20[d]* / *0.48[d]*	*0.34*	*37*	*0.32*	*0.49*	*0.57*	*36*	*0.41*	*1.12*	*0.67*	*27*				
Fe5Co5	1.07	0.34	0.38	22	0.34	0.48	0.45	43	0.31	0.90	0.47	31	0.27	1.72	0.36	4
Fe3.33Co6.67	1.12	0.19	0.24	4	0.34	0.46	0.39	42	0.31	0.87	0.49	44	0.25	1.44	0.47	10
Fe2Co8					0.34	0.45	0.37	40	0.31	0.82	0.40	39	0.25	1.27	0.47	21

[a] Three discrete Lorentzian doublets were considered to characterize the Fe^{3+} phases. For the Fe^{2+} component a quadrupole-splitting distribution was introduced. Oh, octahedral sites; Td, tetrahedral sites; δ, (average) isomer shift (mm/s); ΔE_Q, quadrupole splitting (at the maxima of the distribution) (mm/s); Γ, Lorentzian line width (mm/s); P, proportion (%). The Mössbauer parameters of Fe10 measured at RT (ref 17) are presented in italic for comparison. [b] Isolated ions in MgO (or possibly ions in $MgFe_2O_4$). [c] Ions forming clusters in MgO. [d] Quadrupole-splitting distribution from 0.00 to 1.10 mm/s.
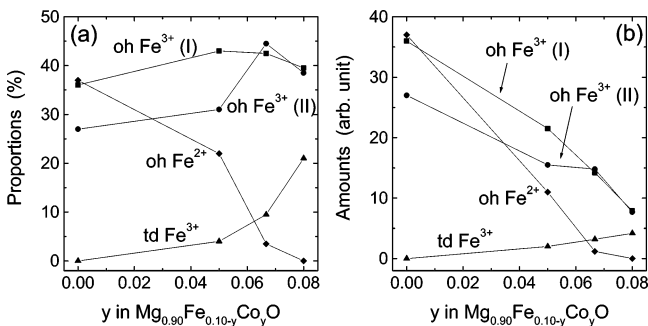
Figure 8. Fractional areas of the different iron sites (a) and amounts of iron in these sites (b) in the oxide powders as revealed by the MS at RT. The amounts were obtained by dividing the corresponding fractional areas by 1, 2, 3, and 5 for Fe10, Fe5Co5, Fe3.33Co6.67, and Fe2Co8, respectively. The lines are guides to the eye.

but the two maxima, ascribed to isolated and clustered Fe^{2+} ions, respectively, appear to be well resolved in the QSD profiles of the latter for all four investigated composite powders. (Table 6). No magnetic splitting due to the Fe^{2+} clusters is observed, in agreement with earlier results.[21]

The second component involves a magnetic phase. The line shape reflects a distribution on the magnetic hyperfine field and its contribution was introduced as such. The relevant adjusted parameters corresponding to maximum probability are included in Tables 5 and 6, column *ferro Fe/Co,* and HFD profiles are reproduced in parts e, h, and k of Figure 9. The parameter values, in particular the hyperfine field H_{hf}, are typical of an α-Fe/Co alloy, showing notably a H_{hf} value that significantly exceeds that of the α-Fe phase present in Fe10R. According to H_{hf}, the alloy possesses an average composition close to α-$Fe_{0.6}Co_{0.4}$ for both Fe5Co5R and Fe3.33Co6.67R and close to α-$Fe_{0.55}$-$Co_{0.45}$ for Fe2Co8R.[51]

The third component is a sextet typical of ferromagnetic Fe_3C and is almost identical to the cementite component resolved from the MS of Fe10R (Tables 5 and 6). Hence, no cobalt seems to be involved in this phase. The fraction of the Fe present in the Fe_3C phase is not affected by the amount of Co in the precursor oxides but is significantly smaller as compared to Fe_3C phase in Fe10R. Hence, the presence of Co, no matter to what extent, triggers the formation of cementite.

Finally, the fourth component appearing in the MS of the composite powders shown in Figure 9 is a singulet exhibiting higher isomer-shift values than that of the γ-Fe–C singlet detected for Fe10R (Tables 5 and 6). The isomer shift of this singlet and its fractional area at RT both increase with the cobalt fraction. For a given Co concentration, the singlet's contribution decreases with decreasing temperature, and this in favor of the magnetic Fe/Co phase. A similar singlet was observed in CNT–Fe/Co–$MgAl_2O_4$ nanocomposite powders[27] and was attributed
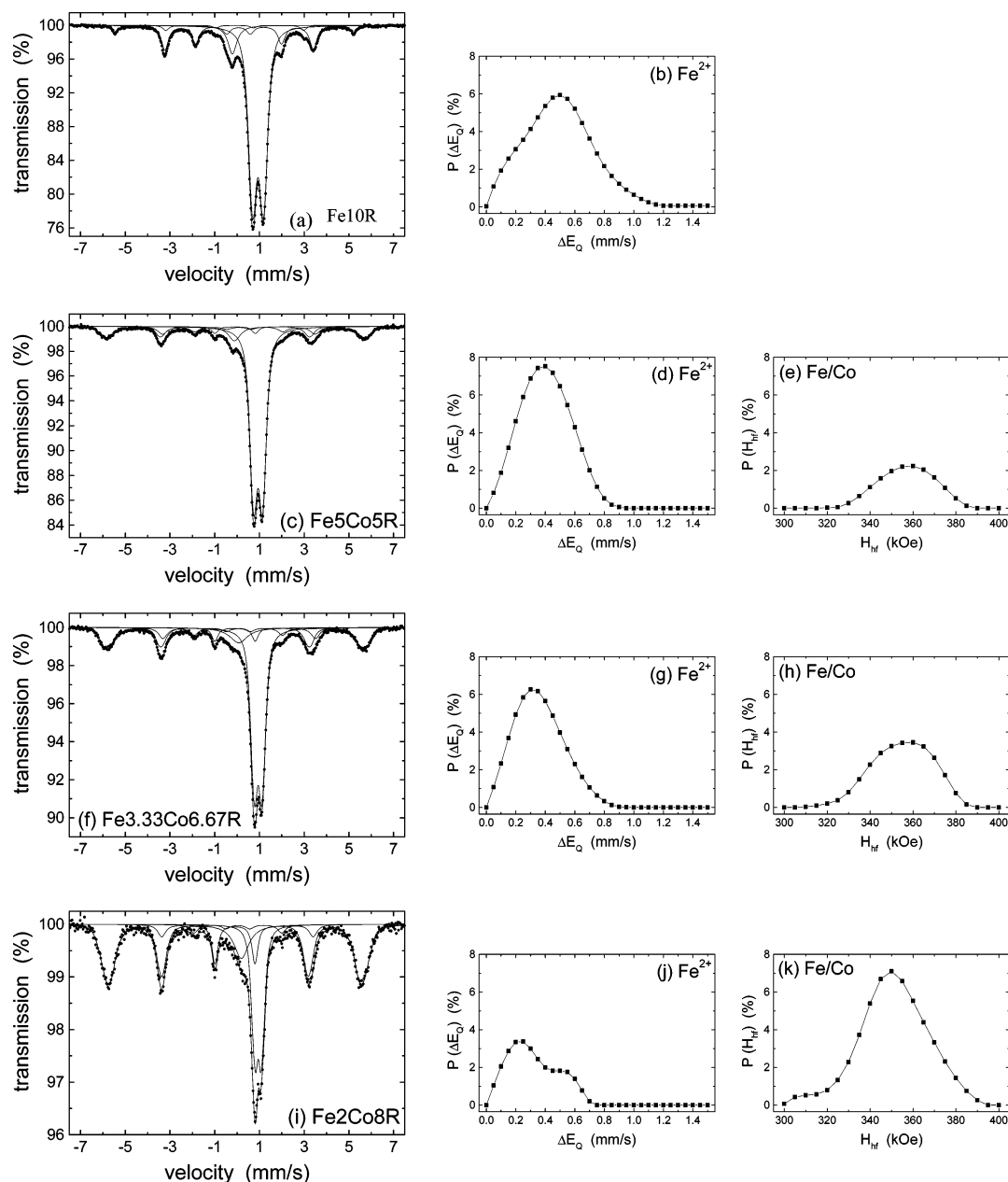
Figure 9. Mössbauer spectra of Fe10R (a), Fe5Co5R (c), Fe3.33Co6.67R (f), and Fe2Co8R (i) measured at RT and corresponding Fe^{2+} quadrupole-splitting distributions ((b, d, g, j, respectively). The hyperfine-field distributions of the ferromagnetic Fe/Co alloys in Fe5Co5R, Fe3.33Co6.67R, and Fe2Co8R (e, h, k, respectively) are also presented.

to superparamagnetic γ-Fe/Co−C particles formed at high temperature and stabilized at RT due to the presence of carbon in the large octahedral voids of the γ fcc structure and to the nanometric size of the particles. It is suggested that the same interpretation holds for the present CNT−Fe/Co−MgO system. The observation that the isomer shift of the γ-Fe/Co−C increases with increasing Co content implies that the Co/Fe ratio of the involved phase changes accordingly. Further, the HFDs evaluated for the Fe/Co magnetic phases are characteristic of ferromagnetic α-Fe/Co as discussed above but, in addition, also contain, especially at 80 K, small contributions due to the magnetic splitting of part of the γ-Fe/Co−C particles.

Discussion

In this section, the formation of the iron(/cobalt) species is discussed in relation with CNTs. Figure 10b shows the fractional spectral areas P of the various iron phases present in the CNT−

Fe/Co−MgO nanocomposite powders versus the cobalt fraction in the corresponding oxide powders (values from Table 5). These P values can be compared with the evolution of the fractional areas of the iron phases in the respective oxide powders presented above (Figure 8) and repeated in Figure 10a for the ease of comparison (values from Table 4).

The Fe^{2+} area fractions are higher in the CNT−Fe/Co−MgO nanocomposite powders than in the corresponding oxide precursors, suggesting a higher Fe-for-Mg substitution degree in the MgO structure for the former. This is in agreement with the higher MgO-lattice parameters observed for the CNT−Fe/Co−MgO nanocomposite powders as compared to the corresponding oxide powders (Table 2), the ionic radius of Fe^{2+} being about 10% larger than that of Mg^{2+}. In accordance with earlier results[21] and with several authors,[44,48,52] it thus appears that Fe^{3+} ions well-dispersed in the Oh sites of precursor MgO tend to form Fe^{2+} ions upon reduction, which at 1000 °C are resistant to

TABLE 5: Mössbauer Parameters of Fe5Co5R, Fe3.33Co6.67R, and Fe2Co8R Measured at RT

composite powder	para Fe^{2+}				ferro Fe/Co (ferro α-Fe)					ferro Fe$_3$C					nonferro Fe (para γ-Fe−C)		
	δ	ΔE_Q	Γ	P	δ	H_{hf}	$2\epsilon_Q$	Γ	P	δ	H_{hf}	$2\epsilon_Q$	Γ	P	δ	Γ	P
Fe10R	*1.04*	*0.20[b] 0.50[b]*	*0.27*	*69*	*0[d]*	*330[d]*	*0[d]*	*0.31*	*5*	*0.18*	*206*	*0.02*	*0.38*	*19*	*−0.10*	*0.48*	*7*
Fe5Co5R	1.05	0.39[c]	0.29	69	0.03	358[e]	0.02	0.32	16	0.19	207	0.00	0.51	9	−0.02	0.64	6
Fe3.33Co6.67R	1.05	0.32² 0.23[c]	0.26	54	0.02	358[e]	0.01	0.30	28	0.18	207	0.04	0.42	10	0.12	0.96	8
Fe2Co8R	1.05	0.50[c]	0.21	28	0.01	350[e]	0.00	0.28	53	0.18	210	0.00	0.41	8	0.21	0.80	11

[a] para, paramagnetic; ferro, ferromagnetic; H_{hf}, hyperfine field (at the maximum of the distribution) (kOe); δ, (average) isomer shift (mm/s); ΔE_Q, quadrupole splitting at the maxima of the distribution (mm/s); $2\epsilon_Q$, (average) quadrupole shift (mm/s); Γ, Lorentzian line width (mm/s); P, proportion (%). The Mössbauer parameters of Fe10R measured at RT are shown in italic to allow comparison. [b] Quadrupole-splitting distribution from 0.00 to 1.50 mm/s [c] Quadrupole-splitting distribution from 0.00 to 1.10 mm/s [d] Fixed parameter [e] Hyperfine-field distribution from 300 to 400 kOe

**TABLE 6: Mössbauer Parameters of Fe5Co5R, Fe3.33Co6.67R, and Fe2Co8R Measured at 80 K[a]**

composite powder	para Fe^{2+}				ferro Fe/Co (ferro α-Fe)					ferro Fe$_3$C					nonferro Fe (para γ-Fe−C)		
	δ	ΔE_Q	Γ	P	δ	H_{hf}	$2\epsilon_Q$	Γ	P	δ	H_{hf}	$2\epsilon_Q$	Γ	P	δ	Γ	P
Fe10R	*1.18*	*0.40[b] 1.03[b]*	*0.33*	*69*	*0.11*	*339*	*0[d]*	*0.32*	*5*	*0.29*	*246*	*0.02*	*0.39*	*20*	*0.01*	*0.45*	*7*
Fe5Co5R	1.16	0.36[b] 0.85[b]	0.28	69	0.14	366[c]	0.01	0.24	18	0.31	246	0.03	0.44	9	0.03	0.47	4
Fe3.33Co6.67R	1.16	0.36[b] 0.85[b]	0.27	56	0.14	364[c]	0.00	0.24	30	0.31	246	0.01	0.38	10	0.18	0.68	4
Fe2Co8R	1.16	0.35[b] 0.83[b]	0.29	29	0.13	357[c]	0.01	0.25	59	0.31	247	0.01	0.35	8	0.30	0.58	4

[a] para, paramagnetic; ferro, ferromagnetic; H_{hf}, hyperfine field (at the maximum of the distribution) (kOe); δ, (average) isomer shift (mm/s); ΔE_Q, quadrupole splitting at the maxima of the distribution (mm/s); $2\epsilon_Q$, (average) quadrupole shift (mm/s); Γ, Lorentzian line width (mm/s); P, proportion (%). The Mössbauer parameters of Fe10R measured at 80 K are shown in italic to allow comparison. [b] Quadrupole-splitting distribution from 0.00 to 2.00 mm/s. [c] Hyperfine-field distribution from 300 to 400 kOe. [d] Fixed parameter.

further reduction to metallic iron.[25] Further, the proportion of Fe^{2+} substituting in the MgO phase present in the nanocomposite powders is observed to decrease drastically with increasing cobalt fraction in the precursor (Figure 10b). This finding is readily understood since, as pointed out earlier, a higher cobalt fraction results in a lowering of the iron ions dispersed in the Oh sites of the parent MgO (Oh Fe^{2+} and partly Oh Fe^{3+} (I) in Figure 10a).

In agreement with previous results[21] and with several earlier reports,[44,46,52] the present findings support the idea that Fe^{3+} clusters and MgFe$_2$O$_4$-like particles tend to be directly reduced to metallic iron, in contrast to the well-dispersed Oh Fe^{3+} ions, which are, as mentioned above, rather resistant to total reduction. Indeed, the increase in the iron fraction involved in the α-Fe/Co phase with increasing Co/Fe ratio (Figure 10b) can be accounted for by the higher abundance in the oxide powders of Td, Oh (II), and, partly, Oh (I) sites occupied by Fe^{3+} (see Figure 10a). It appears that the α-Fe/Co phase in the first place is the result of diffusion of Co^{2+} ions from the MgO lattice into the MgFe$_2$O$_4$-like particles and subsequent reduction of the latter. However, it is plausible that for some reason the MgFe$_2$O$_4$-like particles, or at least a significant fraction of these, more readily interact with the carbon of the reducing atmosphere than with the cobalt substituting in the oxide, resulting upon reduction in the formation of a small proportion of Co-free Fe$_3$C particles which were not detected by the XRD analysis (Figure 5b).

Following the discussion in a report on similar CNTs−Fe/Co−MgAl$_2$O$_4$ nanocomposite powders,[27] it is believed that the γ-Fe/Co−C phase, identified for the present CNT−oxide system, occurs as small particles that are predominantly located
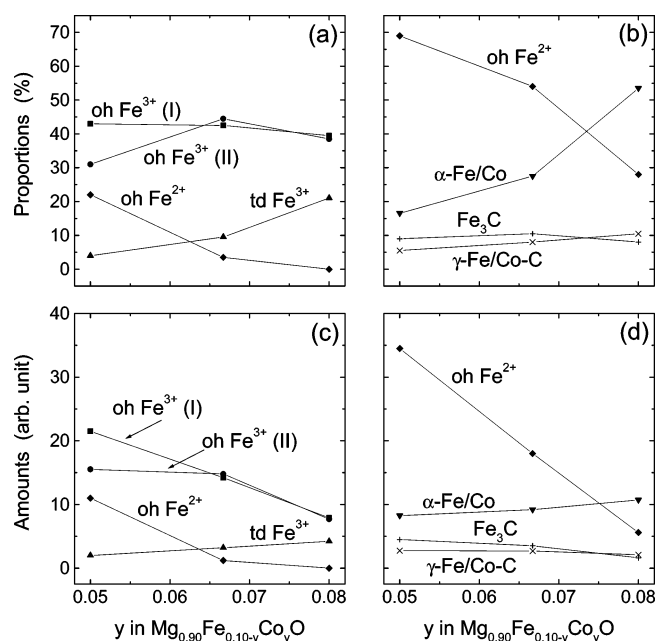
Figure 10. Fractional spectral areas of the different iron sites present in the oxide powders (a) and of the different iron species in the corresponding CNTs−Fe/Co−MgO nanocomposite powders (b), and amounts of Fe in these sites and phases, (c) and (d), respectively, as revealed by the MS at RT. The amounts were obtained by dividing the corresponding fractional areas by 2, 3, and 5 for Fe5Co5(R), Fe3.33Co6.67(R), and Fe2Co8(R), respectively. The solid lines are guides to the eye.

CCVD Carbon Nanotubes in CNT−Fe/Co−MgO

J. Phys. Chem. B, Vol. 109, No. 38, 2005 **17823**

inside the oxide−matrix grains and are as such not directly involved in CNT formation. These particles probably result from the reduction of Co^{2+} and Fe^{2+} ions or from the diffusion of Co^{2+} ions in small Fe^{3+} clusters and subsequent reduction to metallic species.

Dividing the various Fe fractions of Table 5 for Fe5Co5R, Fe3.33Co6.67R, and Fe2Co8R by 2, 3 and 5, respectively, allows direct comparison the absolute amounts of Fe species present in the involved phases constituting the CNT−Fe/Co−MgO nanocomposite powders (see Figure 10d). These amounts referring to Oh Fe^{2+}, Fe_3C, and γ-Fe/Co−C decrease with increasing cobalt fraction, whereas for α-Fe/Co a slight increase is noticed. The latter observation is in line with the XRD patterns of the CNT−Fe/Co−MgO nanocomposite powders (Figure 5b), from which an increase in the amount of α-Fe/Co with increasing cobalt fraction was indeed inferred. Comparing the evolutions of the Fe amounts for the reduced powders (Figure 10d) with those for the parent oxides Fe5Co5, Fe3.33Co6.67, and Fe2Co8 as shown in Figure 10c gives the impression that the iron amount in α-Fe/Co in the composite powders is correlated to the amount of Td Fe^{3+} ions ($MgFe_2O_4$-like phase) in the oxide powders. This would imply that the amount and size distribution of the $MgFe_2O_4$-like particles in the precursors affect the amount and size distribution of the α-Fe/Co particles in the CNT−Fe/Co−MgO nanocomposite powders, taking into account possible coalescence effects upon reduction.

The Mössbauer spectroscopic study of the CNT−Fe/Co−$MgAl_2O_4$ nanocomposite powders[27] showed that the formation of CNTs on Fe/Co−alloy particles occurs without carburization of the catalyst particles and that the CNT quantity has been promoted to the largest extent when an α-$Fe_{0.50}Co_{0.50}$ alloy is detected in the postreaction analysis. In the case of pure iron, however, the formation of Fe_3C poisons the catalyst particles, resulting in a decrease of the CNT quantity and of the carbon quality.[21] The α-Fe/Co amount in the present CNT−Fe/Co−MgO nanocomposite powders increases with increasing cobalt fraction while the Fe_3C amount decreases. Moreover, the composition of the formed alloy is closer to $Fe_{0.50}Co_{0.50}$ with increasing cobalt fraction. This could explain the upgrading of the CNT quantity when the cobalt raises, as observed from Figure 1c. However, the carbon quality for Fe5Co5R, Fe3.33-Co6.67R, and Fe2Co8R (Figure 1d) is similar. Hence, it appears that the higher amount of the $MgFe_2O_4$-like phase with a higher cobalt content in the oxide powders (Figure 10c) generates upon reduction not only more particles with a size adequate for CNT formation but also larger particles responsible for the formation of undesirable carbon species (nanocapsules and fibers). The number of walls and the bundling of the CNTs could also influence the carbon quality. However, the electron microscopy observations do not reveal substantial differences between Fe5Co5R, Fe3.33Co6.67R, and Fe2Co8R in this respect.

In Fe10R, only 20 atom % iron occurs as Fe_3C (Table 5). If one considers an $Fe_{0.50}Co_{0.50}$ composition, the atom % metal (iron and cobalt) involved in α-Fe/Co in Fe5Co5R, Fe3.33-Co6.67R, and Fe2Co8R can be estimated at 16.5, 18.5, and 21.5 atom %, respectively, by multiplying the Mössbauer fractional area of the α-Fe/Co component in Fe5Co5R, Fe3.33Co6.67R, and Fe2Co8R (results from Table 5) by 1, $^2/_3$, and $^2/_5$, respectively. For Co10R, the lattice parameter of MgO (Table 2) indicates that a high proportion of cobalt remains substituted in the MgO lattice upon reduction. A maximum proportion of about 20 atom % cobalt involved in ϵ-Co thus appears to be a plausible estimation. The proportion of metal involved in carbon-filament formation being roughly equivalent in the CNT−Fe−,

CNT−Fe/Co−, and CNT−Co−MgO nanocomposite powders, the presently derived increase in the CNT quantity (Figure 1c) and the global increase in the carbon quality (Figure 1d) reveal notably a better overall dispersion of the metal ions in the oxide precursors. In particular, upon reduction of Co10 ($Mg_{0.9}Co_{0.1}O$ solid solution), the CNTs grow from Co particles that are directly formed from the well-dispersed Co^{2+} ions in MgO. This process appears to be the most efficient one to generate catalyst particles with a size adequate for CNT formation, as witnessed by the high CNT quantity and carbon quality observed for Co10R.

Conclusions

$Mg_{0.90}Fe_xCo_yO$ ($x + y = 0.1$) solid solutions were synthesized by the ureic combustion route. Cobalt ions apparently readily substitute for Mg in the MgO structure so that a single-phase $Mg_{0.90}Co_{0.10}O$ solid solution can be formed. However, it appears that the presence of Co^{2+} ions hinders the dissolution of iron in the MgO lattice, so that an increasing fraction of cobalt in the oxide powders (and thus a decreasing iron fraction) favors the formation and the clustering of Fe^{3+} ions. This results in an increase with the cobalt fraction of the amount and/or size of $MgFe_2O_4$-like particles in the oxide matrixes.

Upon reduction at 1000 °C in H_2−CH_4 of the oxide powders, the Fe^{3+} ions that are well-dispersed in the Oh sites of MgO, tend to form Fe^{2+} ions which are to some extent resistant against reduction to metallic iron. Three reduced phases are detected: α-Fe/Co, Fe_3C, and γ-Fe/Co−C. The $MgFe_2O_4$-like particles in the oxide powders tend to alloy with cobalt upon reduction, forming iron-rich α-Fe/Co particles. These particles are involved in the formation of CNTs (mostly SWNTs and DWNTs with an average diameter close to 2.5 nm) and other carbon species (nanocapsules, fibers), depending on their size. The increasing amount of the $MgFe_2O_4$-like phase with increasing cobalt fraction in the oxides favors the formation of more α-Fe/Co particles with a size and composition (closer to $Fe_{0.50}Co_{0.50}$) adequate for CNT formation. However, at the same time an equivalent proportion of larger particles is produced as well, so that the overall carbon quality in the material remains the same. The highest CNT quantity and carbon quality are eventually obtained upon reduction of the iron-free $Mg_{0.90}$-$Co_{0.10}O$ solid solution, in the absence of clusters of metal ions in the starting material.

References and Notes

(1) Hafner, J. H.; Bronikowski, M. J.; Azamian, B. K.; Nikolaev, P.; Rinzler, A. G.; Colbert, D. T.; Smith, K. A.; Smalley, R. E. *Chem. Phys. Lett.* **1998**, *296*, 195.

(2) Flahaut, E.; Peigney, A.; Laurent, Ch.; Rousset, A. *J. Mater. Chem.* **2000**, *10*, 249.

(3) Bacsa, R. R.; Laurent, Ch.; Peigney, A.; Bacsa, W. S.; Vaugien, Th.; Rousset, A. *Chem. Phys. Lett.* **2000**, *323*, 566.

(4) Peigney, A.; Coquay, P.; Flahaut, E.; Vandenberghe, R. E.; De Grave, E.; Laurent, Ch. *J. Phys. Chem. B* **2001**, *105*, 9699.

(5) Flahaut, E.; Govindaraj, A.; Peigney, A.; Laurent, Ch.; Rousset, A.; Rao, C. N. R. *Chem. Phys. Lett.* **1999**, *300*, 236.

(6) Colomer, J.-F.; Bister, G.; Willems, I.; Konya, Z.; Fonseca, A.; Van Tendeloo, G.; Nagy, B. J. *Chem. Commun.* **1999**, 1343.

(7) Zhu, J.; Yudasaka, M.; Iijima, S. *Chem. Phys. Lett.* **2003,** *380,* 496.

(8) Chiashi, S.; Murakami, Y.; Miyauchi, Y.; Maruyama, S. *Chem. Phys. Lett*. **2004**, *386*, 89.

(9) Kukovecz, Z. N.; Konya, Z.; Nagaraju, I.; Willems, I.; Tamasi, A.; Fonseca, A.; Nagy, B. J.; Kiricsi, I. *Phys. Chem. Chem. Phys*. **2000**, *2*, 3071.

(10) Yang, Y.; Hua, Z.; Lu, Y. N.; Chen, Y. *Mater. Chem. Phys*. **2003**, *82*, 440.

(11) Pinheiro, J. P.; Gadelle, P. *J. Phys. Chem. Sol*. **2001**, *62*, 1015.

(12) Pinheiro, J. P.; Gadelle, P.; Jeandey, C.; Oddou, J. L. *J. Phys. Chem. Solids* **2001**, *62*, 1023.

(13) Avdeeva, L. B.; Reshetenko, T. V.; Ismagilov, Z. R.; Likholobov, V. A. *Appl. Catal., A* **2002**, *228*, 53.

(14) Reshetenko, T. V.; Avdeeva, L. B.; Khassin, A. A.; Kustova, G. M.; Ushakov, V. A.; Moroz, E. M.; Shmakov, A. N.; Kriventsov, V. V.; Kochubey, D. I.; Pavlyukhin, Yu. T.; Chuvilin, A. L.; Ismagilov, Z. R. *Appl. Catal., A* **2004**, *268*, 127.

(15) Reshetenko, T. V.; Avdeeva, L. B.; Ushakov, V. A.; Moroz, E. M.; Shmakov, A. N.; Kriventsov, V. V.; Kochubey, D. I.; Pavlyukhin, Yu. T.; Chuvilin, A. L.; Ismagilov, Z. R. *Appl. Catal., A* **2004**, *270*, 87.

(16) Konya, Z.; Kiss, J.; Oszko, A.; Siska, A.; Kiricsi, I. *Phys. Chem. Chem. Phys*. **2001**, *3*, 155.

(17) Coquay, P.; De Grave, E.; Vandenberghe, R. E.; Dauwe, C.; Flahaut, E.; Laurent, Ch.; Peigney, A.; Rousset, A. *Acta Mater.* **2000**, *48*, 3015.

(18) Peigney, A.; Laurent, Ch.; Dobigeon, F.; Rousset, A. *J. Mater. Res.* **1997**, *12*, 613.

(19) Flahaut, E. Doctoral Thesis, Toulouse (France) 1999.

(20) . Flahaut, E.; Laurent, Ch.; Peigney, A. Nanoengineered Nanofibrous Materials; Guceri, S., Gogotsi, Y. G., Kuznetsov., V., Eds.; Kluwer Academic Publishers: Amsterdam, 2004; pp 35−45

(21) Coquay, P.; Peigney, A.; De Grave, E.; Vandenberghe, Laurent, Ch. *J. Phys. Chem. B* **2002**, *106*, 13199.

(22) Bacsa, R. R.; Laurent, Ch.; Peigney, A.; Vaugien, Th.; Flahaut, E.; Bacsa, W. S.; Rousset, A. *J. Am. Ceram. Soc.* **2002**, *85*, 2666.

(23) Carles, V.; Rousset, A. *Solid State Ionics* **1996**, *83*, 309.

(24) Coquay, P.; De Grave, E.; Peigney, A.; Vandenberghe, Laurent, Ch.; *J. Phys. Chem. B* **2002**, *106*, 13186.

(25) Carles, V.; Brieu, M.; Demai, J. J.; Rousset, A. In *Fourth Euro-Ceramics*; Galassi, C., Ed.; Gruppo Editoriale Faenza Editrice S.p.A.: Faenza (Italy), 1995; Vol. 1, p 323.

(26) Carles, V.; Laurent, Ch.; Brieu, M.; Rousset, A. *J. Mater. Chem.* **1999**, *9*, 1003.

(27) Coquay, P.; Peigney, A.; De Grave, E.; Flahaut, E.; Vandenberghe, Laurent, Ch. *J. Phys. Chem. B* **2005**, *109*, 17825.

(28) Peigney, A.; Laurent, Ch.; Flahaut, E.; Bacsa, R. R.; Rousset, A. *Carbon* **2001**, *39*, 507.

(29) Holland, T. J. B.; Redfern, S. A. T. *Mineral. Magn.* **1997**, *61*, 65.

(30) Vandenberghe, R. E.; De Grave, E.; de Bakker, P. M. A. *Hyperfine Interact.* **1994**, *83*,

(31) Cassell, A. M.; Raymakers, J. A.; Kong, J.; Dai, H. *J. Phys. Chem. B* **1999**, *109*, 6484.

(32) Cheng, H. M.; Li, F.; Sun, X.; Brown, S. D. M.; Pimenta, A.; Marucci, A.; Dresselhaus, G.; Dresselhaus, M. S. *Chem. Phys. Lett.* **1998**, *289*, 602.

(33) Dai, H.; Rinzler, A. G.; Nikolaev, P.; Thess, A.; Colbert, D. T.; Smalley, R. E. *Chem Phys. Lett.* **1996**, *260*, 471.

(34) Kitiyanan, B.; Alvarez, W. E.; Harwell, J. H.; Resasco, D. E. *Chem. Phys. Lett.* **2000**, *317*, 497.

(35) Kong, J.; Cassell, A. M.; Dai, H. *Chem. Phys. Lett.* **1998**, *292*, 567.

(36) Su, M.; Zheng, B.; Liu, J. *Chem. Phys. Lett.* **2000**, *322*, 321.

(37) Cheung, C. L.; Kurtz, A.; Park, H.; Lieber, Ch. M. *J. Phys. Chem. B* **2002**, *106*, 2429.

(38) Flahaut, E.; Peigney, A.; Laurent, Ch. *J. Nanosci. Nanotechnol.* **2003**, *3*, 151.

(39) Kannan R., Pavlovic A. S., Seehra M. S., *J. Phys. C*: *Solid State Phys.* **1986**, *19*, L747.

(40) Berthet, A. Doctoral Thesis; Nancy (France), 1963.

(41) Berthet, A.; Perrot, P. *Mémoires Scientifiques Rev. Métallurg.* **1970**, *LXVII*, 747.

(42) Trinel-Dufour, M. C.; Perrot, P. *Ann. Chim.* **1977**, *2*, 309.

(43) Ingalls, R. *Phys. Rev.* **1964**, *133*, A787.

(44) Boudart, M.; Delbouille, A.; Dumesic, J. A.; Khammouma, S.; Topsoe, H. *J. Catal.* **1975**, *37*, 486.

(45) Jing, J.; Campbell, S. J. *Hyperfine Interact.* **1991**, *68*, 283.

(46) Perez, A.; Marest, G.; Sawicka, B. D.; Sawicki, J. A.; Tyliszczak, T. *Phys. Rev. B* **1983**, *28*, 1227.

(47) Simkin, D. J.; Ficalora, P. J.; Bernheim, R. A. *Phys. Lett.* **1965**, *19*, 536.

(48) Topsoe, H.; Dumesic, J. A.; Derouane, E. G.; Clausen, B. S.; Morup, S.; Villadsen, J.; Topsoe, N. *Stud. Surf. Sci. Catal.* **1979**, *3*, 365.

(49) Waychunas, G. A. *J. Mater. Sci.* **1983**, *18*, 195.

(50) De Bakker, P. Doctoral Thesis; Ghent (Belgium), 1994.

(51) Johnson, C. E.; Ridout, M. S.; Cranshaw, T. E. *Proc. Phys. Soc.* **1963**, *81*, 1079.

(52) Bhide, V. G.; Tambe, B. R. *J. Mater. Sci.* **1969**, *4*, 955.